



Wu, J., Ondra, V., Luebker, J., Kalow, S., Riemenschneider, J., & Titurus, B. (2022). Experimental modal analysis of a rotating tendon-loaded helicopter blade demonstrator. *Mechanical Systems and Signal Processing*, 178, [109286].
<https://doi.org/10.1016/j.ymssp.2022.109286>

Publisher's PDF, also known as Version of record

License (if available):
CC BY

Link to published version (if available):
[10.1016/j.ymssp.2022.109286](https://doi.org/10.1016/j.ymssp.2022.109286)

[Link to publication record in Explore Bristol Research](#)
PDF-document

This is the final published version of the article (version of record). It first appeared online via Elsevier at <https://doi.org/10.1016/j.ymssp.2022.109286>. Please refer to any applicable terms of use of the publisher.

University of Bristol - Explore Bristol Research

General rights

This document is made available in accordance with publisher policies. Please cite only the published version using the reference above. Full terms of use are available:
<http://www.bristol.ac.uk/red/research-policy/pure/user-guides/ebr-terms/>



ELSEVIER

Contents lists available at ScienceDirect

Mechanical Systems and Signal Processing

journal homepage: www.elsevier.com/locate/ymssp

Experimental modal analysis of a rotating tendon-loaded helicopter blade demonstrator

Jun Wu^a, Vaclav Ondra^c, Jannis Luebker^b, Steffen Kalow^b,
Johannes Riemenschneider^b, Brano Titurus^{a,*}

^a Department of Aerospace Engineering, University of Bristol, UK

^b DLR, Braunschweig, Germany

^c Rolls-Royce plc., BS34 7QE, Bristol, UK

ARTICLE INFO

Communicated by Matthias Faes

Keywords:

Rotating beam-tendon
Modal analysis
Whirl tower
Centrifugal stiffening
Compressive softening

ABSTRACT

A novel concept which uses an internal tendon to apply a compressive force on the blades for resonance avoidance of rotorcraft, so-called ‘active tendon concept’, was put forward recently. This research enhances the active tendon concept further toward its basic experimental validation in the rotating operational conditions. To progress in this direction, a new fully dynamically instrumented demonstrator combined with the displacement-based axial load application system is developed and assessed experimentally in non-rotating and rotating conditions for the rotor speeds ranging from 0 rpm to 500 rpm and axial compressive loads ranging from 0 N to 500 N. The identified modal dynamics is used to validate the comprehensive reduced-order model which is subsequently used to support the interpretation of the rotating results where the applied experimental methods lacked in resolution of range.

It is observed that the rotating system features anticipated modal dynamics in the form of centrifugal stiffening and compressive softening of the beam-dominated modes, whilst the tendon-dominated modes display rapid stiffening effects with the applied axial loads. As a result of these opposing trends, further interactional phenomena such as modal veering are observed experimentally and in model-predicted results. One consistently observed beam-dominated mode is used to extend the range of the experimental observations beyond those supported by the models toward the damping characterisation throughout the veering interactions and complex strain mode analysis.

The results presented in this work confirm the anticipated modal behaviour and suggest that the rotating systems can be influenced through controllable preloads whilst in the state of rotation. Additional vibration and load control opportunities arise from the emergent and tunable interactional dynamics between the primary beam or blade system and the secondary augmented tendon preload application system.

1. Introduction

This paper investigates active tendon concept through the analysis of the experimental data collected within the scope of the Shape

* Corresponding author.

E-mail address: brano.titurus@bristol.ac.uk (B. Titurus).

<https://doi.org/10.1016/j.ymssp.2022.109286>

Received 1 February 2022; Received in revised form 4 May 2022; Accepted 5 May 2022

0888-3270/© 2022 The Author(s). Published by Elsevier Ltd. This is an open access article under the CC BY license (<http://creativecommons.org/licenses/by/4.0/>).

Nomenclature

A_B	Cross-sectional area of the beam
E_B, E_L	Young's modulus of the beam and loading box, respectively
G_B	Shear modulus of elasticity of the beam
I_{By}, I_{Ly}	Moment of inertia of the cross-section of the beam and loading box, respectively
k_L	Stiffness of the rotational spring at the root of the loading box
L_0, L_1, L_2	Distance from the rotational center to the blade mounting position, length of loading box, length of the beam, respectively
m_B, m_L, m_T	Mass per unit length of the beam, loading box and tendon, respectively
m_P, m_a	Mass of the tip fixture and the point mass, respectively
P	Applied axial force
t	Time
w_L, w_B, w_T, w_P	Transverse displacements of the loading box, beam, tendon and tip fixture, respectively
α	Coning angle
ρ_B, ρ_L	Density of the beam and loading box, respectively
ψ_B	Rotational angle of the cross-section of the beam due to bending
κ	Shear correction factor of the beam
Ω	Rotational speed

Adaptive Blades for Rotorcraft Efficiency (SABRE) project in collaboration between the University of Bristol (UoB) and the German Aerospace Center (DLR) in Braunschweig. The active tendon concept is intended for resonance avoidance in rotating blades by applying a compressive force to modify the dynamics. Previous works focused on the conceptual theoretical analyses and benchtop experimental studies. The work presented here expands previous research to the experimental campaign completed on the modular demonstrator of the concept integrated with the state-of-the-art rotor rig located at the DLR.

Rotorcraft of all classes and types are subjected to the intense vibratory environment. One of the main sources in this context are the main rotors where symmetrically distributed and rotating blades are exposed to the strong and cyclically repeating aerodynamic excitation [1,2] emerging due to the airflow asymmetry caused by directional flight of the rotating rotor as well as some other sources of such asymmetries (e.g., wake and shed vortices, fuselage interference). Various strategies to control vibration have been historically proposed, ranging from the classical passive dynamic blade design methods [3,4] up to the most recently investigated and promising methods utilising active trailing edge flaps or active blade twist [5]. A particular subset of these methods includes blade-augmented passive, semi-active and active concepts. Examples of these are active pitch links [6], semi-active lead-lag dampers [7] and embedded tuned vibration absorbers [8]. Active tendon concept is specifically intended for future rotor systems which might undergo significant operational changes in their rotor speed [9], blade geometry [10] or even rotor orientation [11]. Furthermore, with their broad range of fluctuating rotor speed and other environmental conditions, it is not inconceivable that this concept could find useful application in wind turbine blades [12] or other aerospace applications beyond rotary wing technologies. Active tendon concept represents a compact method where an axially loaded tendon or multiple tendons deliver a system of compressive loads to the rotating blades in order to alter their dynamic characteristics such as their natural frequencies. The ability to alter, e.g., to decrease, the natural frequencies on demand, gradually or in steps, between different flight or operational regimes can be employed to avoid possible emergent resonant conditions.

Most of the research to date focused on the fundamental aspects such as the experimental benchtop proof-of-the-concept and model development studies. The early experiments and the concept of blade dynamic tuning with the help of compressive loads were originally presented in [13]. The concept was broadly motivated by the work and findings presented in [14,15]. Since then, a range of refined and more detailed investigations were completed both at the levels of the realistically sized simulated rotating blades [16–18] and at the levels of various experimentally validated non-rotating beam configurations [19–21].

To progress the development of the concept, an obvious next step is its experimental demonstration in the rotating state. The analysis of dynamic properties under rotation is extremely demanding and requires significant technical effort. Suitable conditions to complete this analysis were established in the SABRE project through the combined collaborative effort between the UoB and DLR. An advanced state-of-the-art rotor rig located in the DLR Braunschweig was chosen to test the active tendon concept with the help of the dedicated demonstrator. All the previous beam-tendon studies considered only a simple gravity-based loading as a source of the variable axial loads. Due to obvious constraints when testing in the rotating frame of reference, an interchangeable beam-tendon demonstrator was augmented with a compact and manually adjustable loading mechanism which mimics the true active capability.

The aim of this paper is to experimentally demonstrate and validate active tendon concept in the rotating conditions. One objective of the present study is to summarise the identified modal data and, in this way, to evidence the concept characteristics. Another objective is to demonstrate predictive capability of the updated mathematical model. The final objective is to use the focused modal analysis under 2-parameter variations of the rotor speed and applied axial loading to explain the role of modal veering, damping and nonlinearities in the observed structural responses.

This paper is structured as follows: Section 2 introduces the main tools and methods. This includes both detailed description of the new active tendon demonstrator, its preload delivery system, vibration sensing instrumentation as well as detailed definition of the

rotating test environment. To supplement the experiments, this section also introduces the model which is later used to complement and interpret the measured results more confidently. Section 3 presents a systematic summary of the results obtained by the two collaborating organisations. Initial non-rotating tests were completed to provide the high-fidelity experimental data, to interpret the dynamics of new demonstrator comprehensively and to calibrate the mathematical model. A test plan specified for the range of rotor speeds and axial loads is then completed to assess the concept in the rotating conditions. The paper concludes with the analysis and summary of the results assembled throughout this research.

2. Methods

2.1. Rotating active tendon concept demonstrator

The original hypothesis behind this concept was that a tendon can be used to load a rotating blade in compression and produce thus the softening effect opposite the stiffening one arising due to rotation. Such capability could then provide means to control some attributes of the vibration response in the rotating structure. A conceptual outline of such a configuration in the context of a helicopter main rotor blade is shown in Fig. 1.

To study and validate this hypothesis, both theoretically and experimentally, a particular class of compressively loaded beam structures was studied by the authors within the scope of the SABRE project [17,19–21]. Whilst the original idea was inspired by a simple observation that the constant-orientation compressive load, in the lead up to the classical Euler bending buckling, causes reduction of the fundamental natural frequency ultimately toward the zero value when the loss of stability is reached, e.g., [22,23]; the specific frequency-loading characteristics turn out to be closely linked to many other properties. Examples of these are the orientation of the resultant compressive force, the sectional tendon placement relative to the cross-section itself, various linearity assumptions such as those associated with negligibly small changes in the magnitude of the axial force, or nature of the beam-tendon spanwise interactions. For instance, it was shown that the sensitivity of the natural frequencies to the tendon forces significantly decreases with increasing number of the tendon-guiding elements and the trend can be completely reversed (i.e., increasing natural frequencies with the applied load) when follower forces are considered [21] or when the tendon is not coincident with the shear centre of the beam cross-section [20]. Further localised effects are associated with the beam-tendon dynamic coupling observed during certain loading regimes where phenomena such as modal veering cause inter-modal coupling between the beam and tendon dynamics resulting in locally non-monotonous frequency-loading trends and experimentally observed activation of the non-proportional damping at the beam-tendon interfaces.

All previous studies focused on investigations in the nonrotating and highly controlled laboratory conditions. The rotating demonstrator was designed to enable introduction of the adjustable axial tendon preloads as well as application of the modal test inputs in the rotating frame of reference. Initially, the demonstrator was comprehensively tested in the nonrotating benchtop configuration in the BLADE lab at the University of Bristol, U.K. (UoB test configuration), with the main objective being comprehensive determination of the nonrotating modal characteristics, evaluation of the boundary conditions and validation of the reference mathematical model. After this, the demonstrator was tested on the rotating whirl tower at the DLR in Braunschweig, Germany (DLR test configuration), with the main objective being experimental validation of the operational principles and mechanics.

2.2. Rotating beam-tendon demonstrator

2.2.1. Test configurations

A schematic outline of the complete system in its DLR test configuration is shown in Fig. 2. In contrast with the previous research where the beam compression was applied directly via the tendon and the gravity-loaded pulley system, e.g. [24], the present demonstrator integrates an additional part in the form of the loading box which enables an indirect displacement-based load control

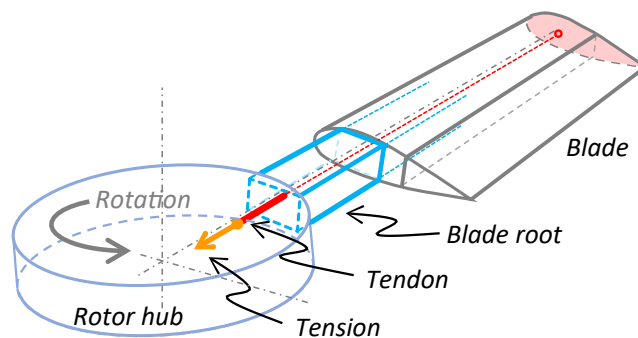


Fig. 1. Conceptual scheme of the active tendon incorporated within a rotating blade.

achieved by a custom-made turnbuckle mechanism causing elastic axial prestress in the tendon-beam system. The demonstrator was designed and operated such that, through the application of small vibrations and careful design decisions, the linearity, constant preload and small damping assumptions remained approximately satisfied throughout the tests.

Focusing on the UoB part of the system, the demonstrator consists of the two main parts, the loading box and the tendon-beam assembly. The loading box not only enabled the axial preloading, but it also formed the key load-bearing structure which transmitted all loads including the centrifugal loads and dynamic bending loads. Owing to its finite flexibility, the loading box influenced appreciably the overall dynamics of the tested system. A single dominant vibration plane perpendicular to the plane of rotation (i.e., out-of-plane or flapping vibration) was promoted by design. A rectangular aluminium profile with the softer out-of-plane bending direction was used to achieve this as well as to minimise any unwanted effects such as gyroscopic in-plane response. To minimize the influence of induced aerodynamic effects, the rectangular beam cross-section was streamlined in the direction of rotation with the help of the semi-circular acrylic fairing establishing thus an aerodynamic contour with a single axis of symmetry. This approach helped to reduce the effect of shed sectional vorticity and induced steady as well as oscillatory components of the aerodynamic loads, simplifying thus the identification process.

A beam with a tendon freely passing through the entirety of the beam was tested, and the tendon was further guided into the loading box. The calibrated turnbuckle mechanism was used to vary the axial strains, and thus the loads, within the closed-circuit system consisting of the beam, tendon and loading box. During the rotating tests, the loads were manually set by following the prescribed prestressing protocol between the individual rotor speed sweeps. Otherwise, the tendon-loaded beam design broadly followed the architecture already previously studied in the laboratory conditions in [19,24]. Both test configurations are shown in Fig. 3.

The loading box constituted an external interface with the attachment fixture in the UoB installation, Fig. 3a), and the rotor hub in the DLR installation, Fig. 3b). In case shown in Fig. 3a), the demonstrator was fixed to the stiff laboratory tabletop using a solid steel column and a pair of M13 steel bolts. The DLR rotor rig is described in the following section. Whilst not identical, these two test configurations provided comparable boundary conditions as is shown later in this paper.

2.2.2. DLR rotor rig

The active tendon demonstrator described in the previous section was tested in the DLR Whirl tower shown in Fig. 3b). The test rig has undergone a deep renovation over the last few years and the test campaign presented in this paper was also one of its main initial runs. The loading box was attached to the blade arm of the DLR rotor head using the two 15 mm diameter steel shoulder bolts. The blade arm was fully articulated, i.e., allowing free flap or out-of-the-plane and lead-lag or in-plane motions of the test articles. Whilst not used in this experiment, the rig was also equipped with a provision for automatic pitch control. The breakdown of the rig is presented in Fig. 4.

As shown in Fig. 4a), the rig consists of a concrete base (blue), torque monitoring unit (green), balance monitoring unit (yellow), motor (orange), rotor head (red). As further detailed in Fig. 4b), the rotor head consists of an angular encoder (red), electrical slipping

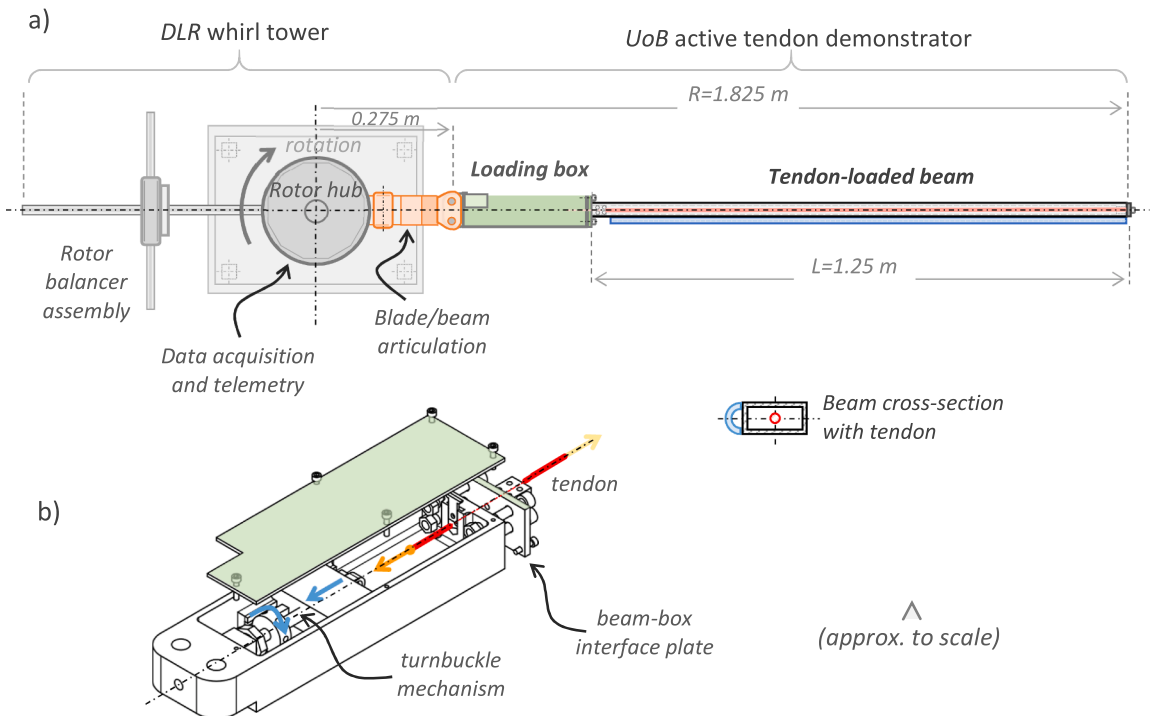


Fig. 2. The rotating active tendon demonstrator: a) top view, b) loading box detail.

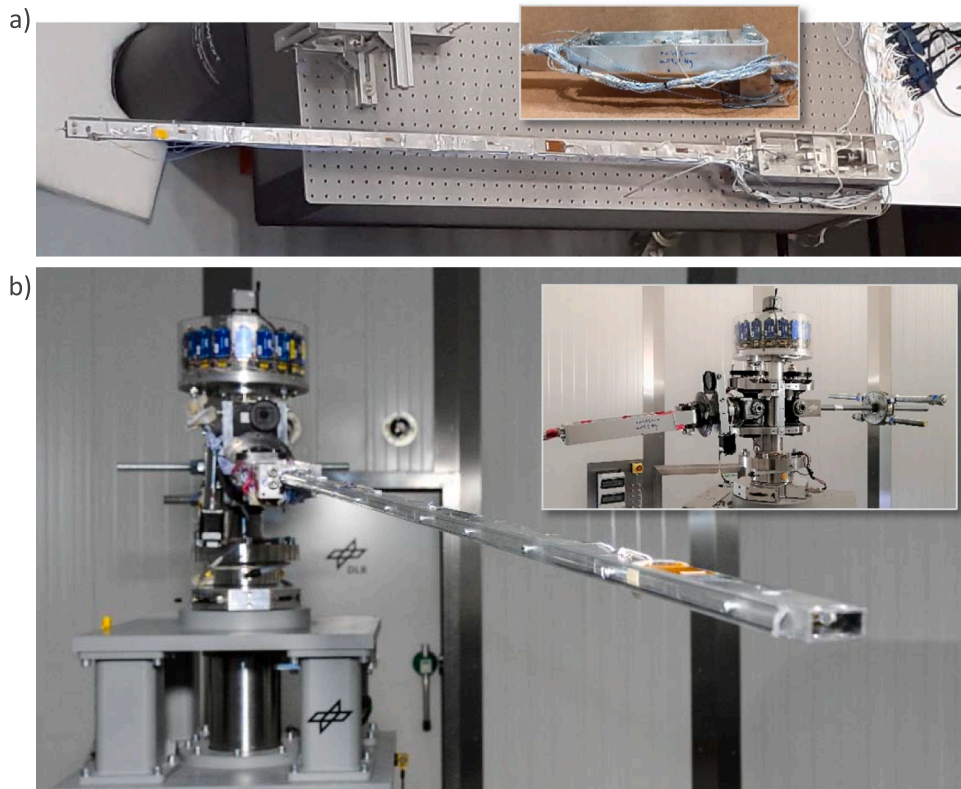


Fig. 3. Active tendon demonstrator configurations: a) UoB laboratory installation – top view, inset: loading box – side view, b) DLR whirl tower installation, inset: rotor head detail.

(green), pitch control (purple), balancing arm (orange), telemetry module (blue) and blade arm (yellow). Both the rotating and the non-rotating parts of the setup were equipped with various measurement systems. For completeness, these are detailed in Appendix B. The resulting measured signal channels are shown in Fig. 4c). Among these, mainly the channels 1–5, 8, 9, 19 and 20 are used in the subsequent dynamic analysis. The whole signal set, however, was used throughout the test campaign to control the test rig and ensure the required test conditions were implemented satisfactorily.

The test stand was designed to operate with a single test specimen mounted to the blade arm while the balancing mechanism was

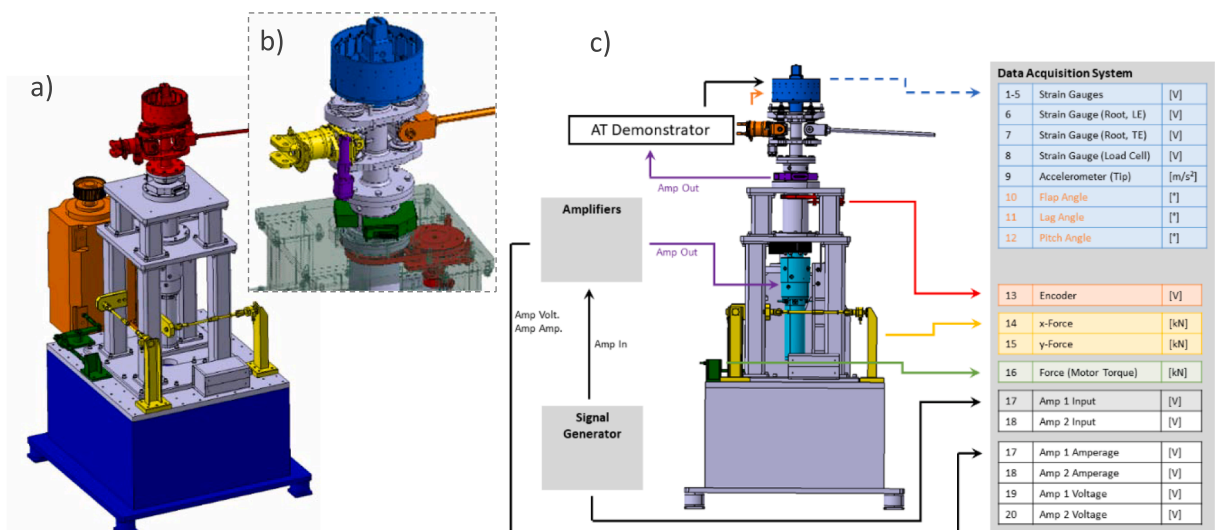


Fig. 4. The DLR Whirl tower: a) full test stand, b) rotor head detail, c) measurement and actuation signals (dashed lines indicate wireless telemetry).

located on the opposite side of the rotor. The rotor rig is powered by a motor with the maximum output of $P_{Motor} = 48$ kW and it can operate at the rotation speeds up to $n_{max} = 3000$ rpm. The rotor rig is located on a massive concrete base and this base is mechanically de-coupled from the test chamber structure via four elastomeric dampers placed at each corner of the base to decrease vibration transmission coming from the outside environment. Further details regarding the modal test procedure are provided in the following sections.

2.3. Experimental methods

The input–output suite for the demonstrator was designed with the primary focus on the rotating tests. The associated equipment was therefore permanently integrated with the tested structure. Additional and supplementary dynamic testing on the non-rotating demonstrator was completed with the help of an impact hammer. The combined view of the DLR and UoB input–output locations is provided in Fig. 5.

This figure includes piezo-patch and strain gauge information used during the DLR rotating tests as well as the locations of the impact hammer inputs used during the UoB nonrotating tests. The reference accelerometer was shared between both test configurations.

2.3.1. DLR rotating modal test

After mounting the demonstrator (Fig. 3b)), the rotor rig balancing was performed using the DLR vibration analyzer (Vibrex 2000). Further, the strain gauges in the loading box were calibrated using the gravity weights attached to the tendon at the demonstrator’s tip through the pulley mechanism used to redirect the load from the vertical to the radial direction. The weights were increased/decreased stepwise, to/from the maximum loading value, to estimate the load monitoring system’s strain sensitivity using the recorded strain-force relationship. For carrying out the actual test runs, the nominal force was set manually before each automated rotor speed sweep by using the load adjustment turnbuckle mechanism.

To excite the beam in the rotating or stationary state, a pair of piezoelectric patches (type: Smart Material M2814-P1) was glued onto the upper and bottom surfaces of the beam. The location of the patches was selected to avoid the strain nodes of the first five beam modes. The excitation signal of the piezoelectric patches was a conditioned sweep sine signal generated by an *Ono Sokki* analogue I/O FFT analyser CF-7200 and amplified by Trek PZD2000A High Voltage Amplifiers. The signal was fed into the two patches out-of-phase, so that the bending moment could be generated across the beam’s thickness. As also shown in Figs. 4 and 5, the control signals of the amplifier were also recorded by NI PXIe-8135 system with a NI PXIe-6355 data acquisition device for later frequency response function calculations.

Overall, there were five half-bridges spaced along the tested beams, each consisting of two strain gauges (type: HBK 1-LY41-6/350) glued onto the upper and lower surfaces of the beams. The half-bridges were used to measure the bending strains of the beam and had the functions of cancelling axial strain and temperature change. The two strain gauges located in the loading box (type: HBK 1-LY41-6/350) formed a single half-bridge which was used to monitor the applied axial force in the tendon and had the function of cancelling temperature changes. The strain signals were acquired by the data acquisition system via the dedicated strain gauge modules (KMT32 Mini Telemetry modules for strain gauges). A single-axis accelerometer (PCB 352A25) positioned close to the beam tip was used to measure the flapping acceleration in the rotating frame of reference. The resulting data were acquired by the data acquisition system via KMT MT32 Mini Telemetry modules for the ICP devices.

After the steady rotational test conditions were achieved, the sine sweep excitation was used to excite the vibration responses in the focused way in otherwise significantly challenging and noisy rotating test environment. To further enhance excitation control, the two excitation sweeps were completed at every rotation speed. Each first run had the maximum frequency of 500 Hz, whereas the second

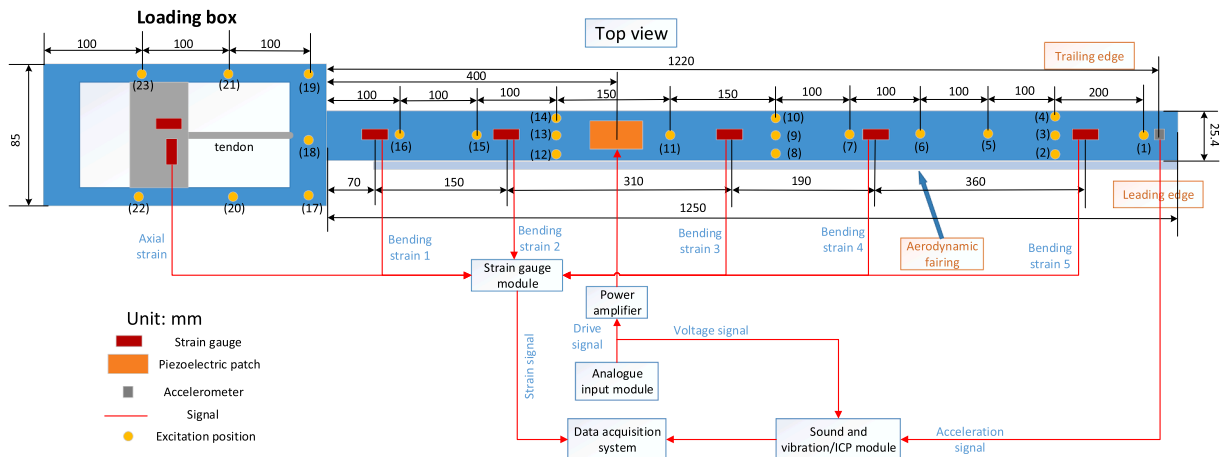


Fig. 5. Signal input–output layout during the nonrotating and rotating tests.

run was limited to the frequency of 64 Hz. Whilst the total duration was 30 s, each former sweep lasted 4.2 s, and each latter lasted 15 s. The two controlled experimental parameters were the applied tendon force and the rotor speed. To cover a wide range of the test conditions, 42 test cases were defined according to the test matrix shown in Fig. 6.

Where required, the recorded input and output signals were detrended, despiked and further processed in the Matlab working environment. Specifically, any undesired signal outliers occurring in the form of signal spikes were eliminated with the judicious use of filloutliers function. The frequency response functions (FRFs) from the piezo-patch excitation (assumed as the half of the difference between the two input voltage signals (channels 19 and 20 in Fig. 4c)) to the response signals (the tip acceleration (channel 9) and bending strains (channels 1–5)) were calculated using tfestimate function with 50% overlap and Hanning window. These FRFs were then used for identification of the system’s modal properties in the frequency domain and their changes with the applied axial forces and rotor speeds. The modal identification was conducted using the combination of PolyMAX [25] and least square based modal pole-residue parameterisation [26] techniques. Having performed analysis in the frequency domain, any transfer function artefacts associated with the rotor speed harmonic frequencies were ignored and only the modes of interest observed in the nonrotating conditions were included in the identification.

2.3.2. UoB nonrotating modal test

The demonstrator was tested in the nonrotating conditions using the refined test grid (0–600 N with an increment of 10 N each time). As shown in Fig. 3a), the fixed boundary conditions closely approximated the DLR test specimen conditions. The influence of the rigid body articulation, when inserted in the DLR rotor arm, arising due to the rotor head mechanical flapping hinge was not replicated because this feature, in this setup, did not appreciably influence the flapping beam-tendon dynamics of interest.

The focus was placed on the influence of the loading box on the modal dynamics of the active tendon demonstrator. The objective, at this stage, was a comprehensive mapping of the nonrotating modal characteristics, analysis of any possible interaction between the loading box and the tendon-loaded beam, and validation of the mathematical model. The demonstrator was tested in the fully assembled state including the aerodynamic fairing, strain gauges, piezo patches and associated taped cabling.

An impact hammer (PCB 086C01) was used to excite the demonstrator at the 23 positions shown in Fig. 5 while the same single-axis miniature accelerometer (PCB 352A25) was placed at the same reference tip position to measure the acceleration. Both the hammer force and acceleration were acquired by NI data acquisition system via NI 9234 module. The FRFs from the hammer input to the acceleration were calculated. The test conditions were set up such that the nominal frequency range up to 500 Hz could be investigated and the modal properties were identified by the PolyMAX method [25]. To obtain the strain mode shape for further comparison with the rotating tests, the bending strains from the five half-bridges were measured when the beam was excited by the hammer at the position 6 (see Fig. 5). The strain signals were acquired by NI data acquisition system via NI 9237 module. In this case, also the PolyMAX method was used.

2.4. Mathematical model

Previously developed mathematical model [24,27] is extended here by considering the specifics of the tested configurations (Fig. 7). Previous formulation [24] is extended by including the influence of the loading box and a non-zero coning angle (an angle between the straight undeformed beam and the plane perpendicular to the rotation axis) arising due to the residual steady lifting loads is also considered. These additions allow further tuning of the model to the specific test conditions.

The aerodynamic forces in this model are neglected. Only the vibration in the flapping direction is considered. The influence of the flexibility of the whirl tower is not considered.

The resulting modelled system is shown in Fig. 7. The hollow rectangular cross-sectional beam is connected with a tendon at the tip

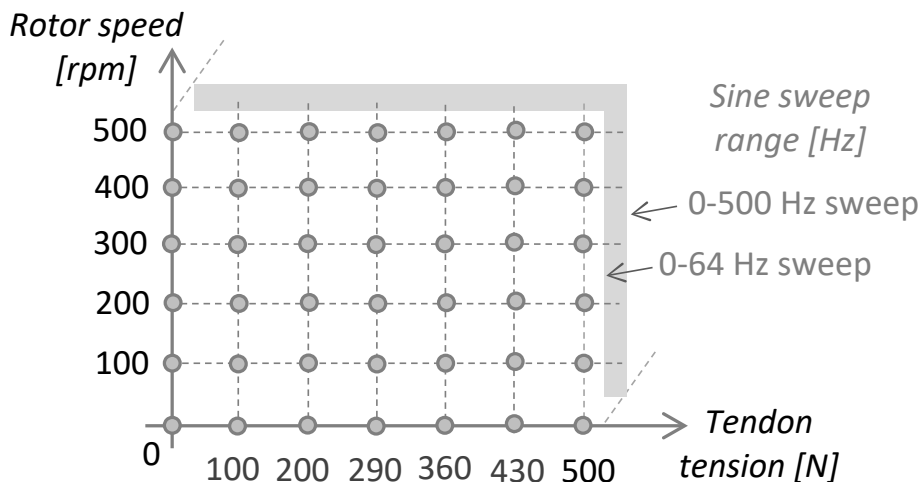


Fig. 6. The complete load-speed test matrix.

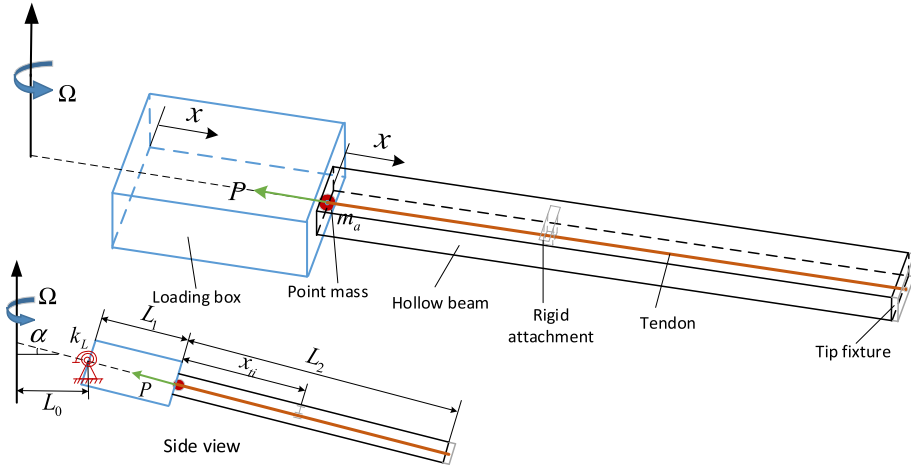


Fig. 7. The extended loading box-beam-tendon model.

using a tip fixture. The tendon is coincident with the elastic axis of the beam in the undeformed position. Owing to its high bending stiffness and the presence of only a single loading box mode in the frequency range of interest when studied in isolation from the beam the loading box is modelled using the Euler-Bernoulli beam assumptions. On the other hand, the beam and tendon are modelled as Timoshenko beam and string, respectively. The tendon is loaded with a constant tension P that acts as a compressive axial force applied to the beam. The loading box and beam-tendon system is rotating with a constant rotational speed Ω with a coning angle α . The loading box is simply supported at the root, where it is also constrained by a rotational spring k_L to accommodate the different boundary conditions. The beam is attached to the loading box at their common interface, where the tendon is also constrained to have the same deflection as the beam. A point mass (m_a) is added at the root of the beam to take into account the additional mass at their connection interface.

Given the chosen modelling approach, the transversal deformation of the loading box $w_L(x, t)$, the transversal deformation and sectional rotation of the beam $w_B(x, t)$ and $\psi_B(x, t)$, respectively, and the tendon transversal deformation $w_T(x, t)$ are discretised as follows.

$$\begin{aligned}
 w_L(x, t) &= \sum_{i=1}^{N_L} W_{Li}(x)q_{Li}(t) = \mathbf{q}_L(t)\mathbf{W}_L(x), \quad w_B(x, t) = \sum_{i=1}^{N_w} W_{Bi}(x)q_{Bzi}(t) = \mathbf{q}_{Bz}(t)\mathbf{W}_B(x) \\
 \psi_B(x, t) &= \sum_{i=1}^{N_r} \Psi_{Bi}(x)q_{Bri}(t) = \mathbf{q}_{Br}(t)\mathbf{\Psi}_B(x), \quad w_T(x, t) = \sum_{i=1}^{N_{wt}} W_{Ti}(x)q_{Ti}(t) = \mathbf{q}_T(t)\mathbf{W}_T(x)
 \end{aligned}
 \tag{1}$$

where $W_{Li}(x)$, $W_{Bi}(x)$, $\Psi_{Bi}(x)$ and $W_{Ti}(x)$ are the normalised orthogonal polynomials for the transverse displacement of the loading box, transverse displacement and sectional rotation of the beam, and transverse displacement of the tendon, respectively. They are generated by the Gram-Schmidt process with the following geometric or essential boundary conditions: $w_L(0) = 0$. The functions $q_{Li}(t)$, $q_{Bzi}(t)$, $q_{Bri}(t)$, and $q_{Ti}(t)$ are the generalised time-dependent coordinates.

The total kinetic energy and potential energy expressions for the box-beam-tendon system are.

$$\begin{aligned}
 T &= T_L + T_a + T_B + T_T + T_P, \\
 U &= U_L + U_B + U_T + U_{c1} + U_{c2} + U_{c3} + U_{cf} + U_{cl}
 \end{aligned}
 \tag{2}$$

where T_L , T_a , T_B , T_T , and T_P are the kinetic energies of the loading box, point mass, beam, tendon and tip fixture, respectively, while U_L , U_B , U_T , U_{c1} , U_{c2} , U_{c3} , U_{cf} , U_{cl} are the potential energies due to the loading box, beam, tendon, the connection between the beam and tendon at the tip via the tip fixture, the connection between the loading box and beam, the connection between beam and tendon at the root, the connection between beam and tendon via the rigid attachment, and the rotational constraint of the loading box, respectively. The specific energy expressions can be discretised using the functional series introduced in Eq. (1) and the resulting equations of motion are obtained with the help of the Lagrange's equation of the second kind.

$$\frac{d}{dt} \left(\frac{\partial T}{\partial \dot{\mathbf{q}}} \right) - \frac{\partial T}{\partial \mathbf{q}} + \frac{\partial U}{\partial \mathbf{q}} = \mathbf{0}
 \tag{3}$$

where $\mathbf{q} = [q_L \quad q_{Bz} \quad q_{Br} \quad q_T \quad w_P]$ is the $N_L + N_w + N_r + N_{wt} + 1$ generalised coordinate vector of the full box-beam-tendon system. This approach yields the resulting in-vacuo equations of motion written in the compact matrix form.

$$\mathbf{M} \ddot{\mathbf{q}}^T + \mathbf{K} \mathbf{q}^T = \mathbf{0}
 \tag{4}$$

where the mass matrix M and stiffness matrix K

$$M = \text{diag}([M_L, M_B + M_a, M_T, m_p]), \quad K = \text{diag}([K_L, K_B, K_T, 0]) + K_c \quad (5)$$

consist of the following block matrices

$$K_L = K_{L1} + \Omega^2 K_{L3} - \Omega^2 K_{L4} - PK_{LP}, \quad K_B = K_{B1} + K_{B2} + \Omega^2 K_{B3} - \Omega^2 K_{B4} - PK_{BP}, \\ K_T = \Omega^2 K_{T3} - \Omega^2 K_{T4} + PK_{TP}, \quad K_c = K_{c1} + K_{c2} + K_{c3} + K_{cf} + K_{cl} \quad (6)$$

and where $\text{diag}(\cdot)$ is a block diagonal matrix; L, B, T, c subscripts denote the loading box, beam, tendon and coupling terms, respectively. The two primary control parameters in the following studies are the tendon axial force P and the rotor speed Ω .

These component matrices provide a clear links between the various physical effects and individual equation terms. The detailed process of derivation as well as the specific content of all individual matrices are given in Appendix A.

The parameters, including the mass per unit length of the beam and loading box (m_B, m_L), the bending rigidities of the beam and loading box ($E_B I_{By}, E_L I_{Ly}$), the shear modulus of the beam (G_B), the mass of the point mass (m_a), the rotational spring (k_L) and the mass of the tip fixture (m_p) was updated by minimizing the error between the complete model and experimental data in terms of the natural frequencies of the nonrotating unloaded beam, and the error for the isolated loading box model, using the optimization strategy adopted from [28].

3. Results

3.1. UoB nonrotating modal analysis

3.1.1. Baseline nonrotating modal characteristics

To illustrate the typical modal content observed in the nonrotating conditions, Fig. 8 shows an example of the unloaded and fully loaded case of the accelerance FRF identified between the accelerometer location and the hammer input position 6 (Fig. 5). It is interesting to contrast these results with those made on the previous gravity loaded test setups [19,24].

The unloaded case (0 Newtons) features modes which involve only the beam activity. The first five main bending modes are denoted by B1 to B5. Due to the presence of the loading box and its clamping setup, a previously not observed “box mode” is found close to 86.5 Hz. Another newly observed mode is located close to 359 Hz. This is a “torsional mode” and it is present within the frequency range of interest due to the relative torsional softness originating from the loading box combined with a slightly asymmetric attachment of the beam to the loading box. Owing to the used input–output combination, the evidence of this mode is only minimally present in the shown FRF. These two modes will be more closely described in the following discussion focused on the mode shape characteristics.

Compared with the previous unloaded instance, the fully loaded case (600 Newtons) features the additional modes evidencing the tendon-dominated dynamics. These modes are denoted T1 to T6 and they are highly sensitive to the level of the applied tensile loading. Note that the maximum load was limited to 500 Newtons during the rotating tests and B1 mode turned out to be significantly affected by the noisy test conditions present during the rotating tests.

Table 1 provides systematic description of the identified modal properties for the two extreme loading cases. The identified undamped natural frequency, damping ratio and mode shape are provided for each case. Because the tendon was not instrumented, all shown modes contain only the loading box and beam input locations consistent with Fig. 5. The identified modes are very close to the real or normal modes due to the small levels of damping present in the nominal nonrotating system.

Modes B1 to B5 feature classic cantilevered beam bending patterns, with generally negligible torsional content, and with progressively increasing number of nodal points when the mode order increases. Except for mode B3 at 600 N, the modal activity in the loading box region is also negligible. Modes T1 to T6 are the tendon-dominated modes. However, this aspect of their behaviour is not visible in Table 1 because the tendon was not instrumented during the tests, and this is where the model will be used to complement the observed results.

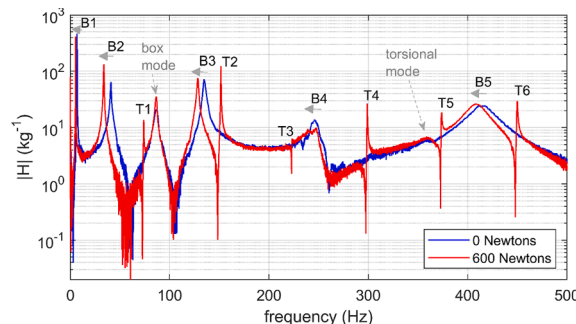
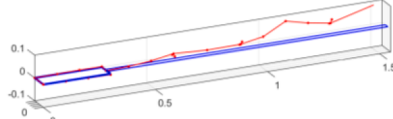
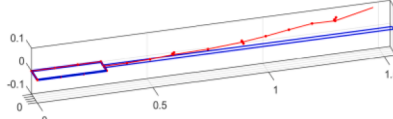
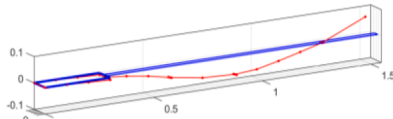
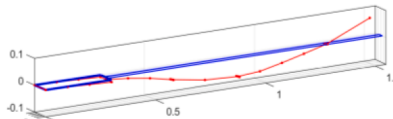
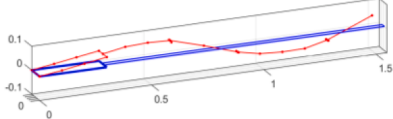
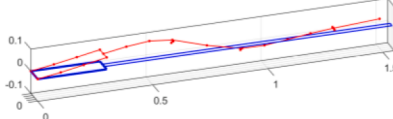
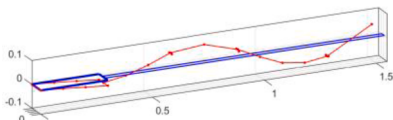
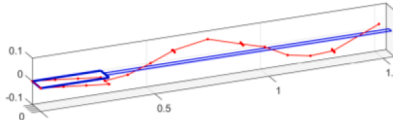
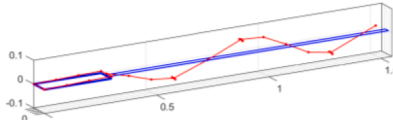
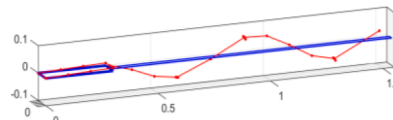


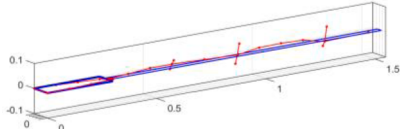
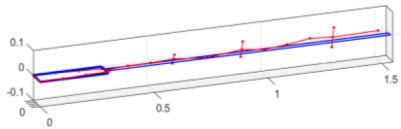
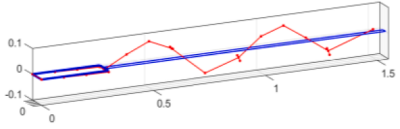
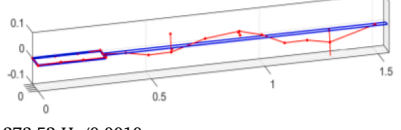

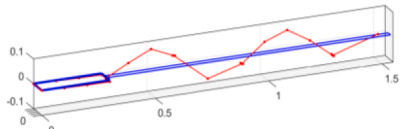
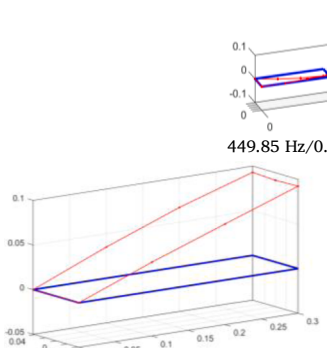
Fig. 8. Comparison between unloaded and fully loaded test structure.

Table 1
3D experimental modes (frequency and damping ratio separated by slash) of the demonstrator for the two axial forces.

Mode	0 N	600 N
B1		
	6.83 Hz / 0.0020	5.31 Hz / 0.0031
B2		
T1	40.88 Hz / 0.019 N/A	33.71 Hz / 0.0069
Box mode		
	86.48 Hz / 0.019	73.78 Hz / 0.0045
B3		
	134.96 Hz / 0.0094	86.30 Hz / 0.0106
T2	N/A	128.26 Hz / 0.0066
T3	N/A	151.59 Hz / 0.0009
B4		
	246.16 Hz / 0.0164	223.01 Hz / 0.0034
T4	N/A	247.82 Hz / 0.0133
Torsion mode		298.98 Hz / 0.0006

(continued on next page)

Table 1 (continued)

Mode	0 N	600 N
T5	 <p>362.43 Hz / 0.0223 N/A</p>	 <p>364.17 Hz / 0.0185</p>
B5	 <p>415.43 Hz / 0.0306 N/A</p>	 <p>373.52 Hz / 0.0010</p>
T6	 <p>415.43 Hz / 0.0306 N/A</p>	 <p>409.54 Hz / 0.0241</p>
Isolated loading box		 <p>449.85 Hz / 0.0008 106.36 Hz / 0.0102</p>

Whilst separated well from the neighbouring bending modes, the box mode features the heightened activity in the loading box region combined with the key characteristics of B3 mode. From Table 1, it can also be seen that this mode’s box region is relatively undeformed, and the mobility emerges from the root region where the box is clamped to the table. An independent study aimed at the behaviour of the loading box in isolation, under the influence of the same clamping conditions, confirmed this conclusion and the first loading box mode is also included in Table 1. This mode is successfully predicted in the next section, and it is shown to be relatively insensitive to the applied axial loading. Finally, the torsional mode features notable torsional activity distributed across its loading box and beam segments. Owing to the focus of this paper, this mode is not modelled and studied in this work.

3.1.2. Model-experiment correlation

This section demonstrates validity of the model introduced in section 2.4 and Appendix A. As well as validity check, this section further serves to gain a deeper insight into the modal characteristics and to support the rotating configuration analysis. The model

Table 2
Model parameters.

Parameter	Value, unit	Parameter	Value, unit
L_0	0.275 m	$E_L I_{Ly}$	3600 Nm ²
L_1	0.3 m	m_T	0.017 kg/m
L_2	1.25 m	k_t (UoB, DLR tests)	3.62×10^4 Nm/rad
E_B	69 GPa	m_p	0.028 kg
A_B	11.16×10^{-5} m ²	m_a	0.171 kg
m_B	0.287 kg/m	k	1×10^8 N/m
$E_B I_{By}$	138.87 Nm ²	k_r	1×10^8 Nm/rad
G_B	30.56 GPa	$N_w/N_r/N_{wt}/N_L$	15 / 15 / 18 / 5
κ	0.5	α (UoB test)	0 deg (horizontal)
m_L	5.18 kg/m	α (DLR test)	0 deg (assumed)

parameters are summarised in Table 2. Where possible, the parameters were directly measured or collected. The parameter values for m_B , m_L , $E_B I_{By}$, $E_L I_{Ly}$, G_B , m_a , k_L and m_p were obtained using the parameter updating procedure outlined at the end of section 2.4.

The analysis provided in this section considers mainly the characteristics of the undamped system. The highest identified modal damping values are observed at mode B5 with the value of 2.4–3 % and all other damping ratio values are around 1 % or less. The 600 N test case is used in this study and the model enables presentation of the unmeasured tendon dynamics in B1 to B5 modes. In addition to the displacement mode shapes, this section also presents the strain modes recovered from the strain gauge locations during the impact tests.

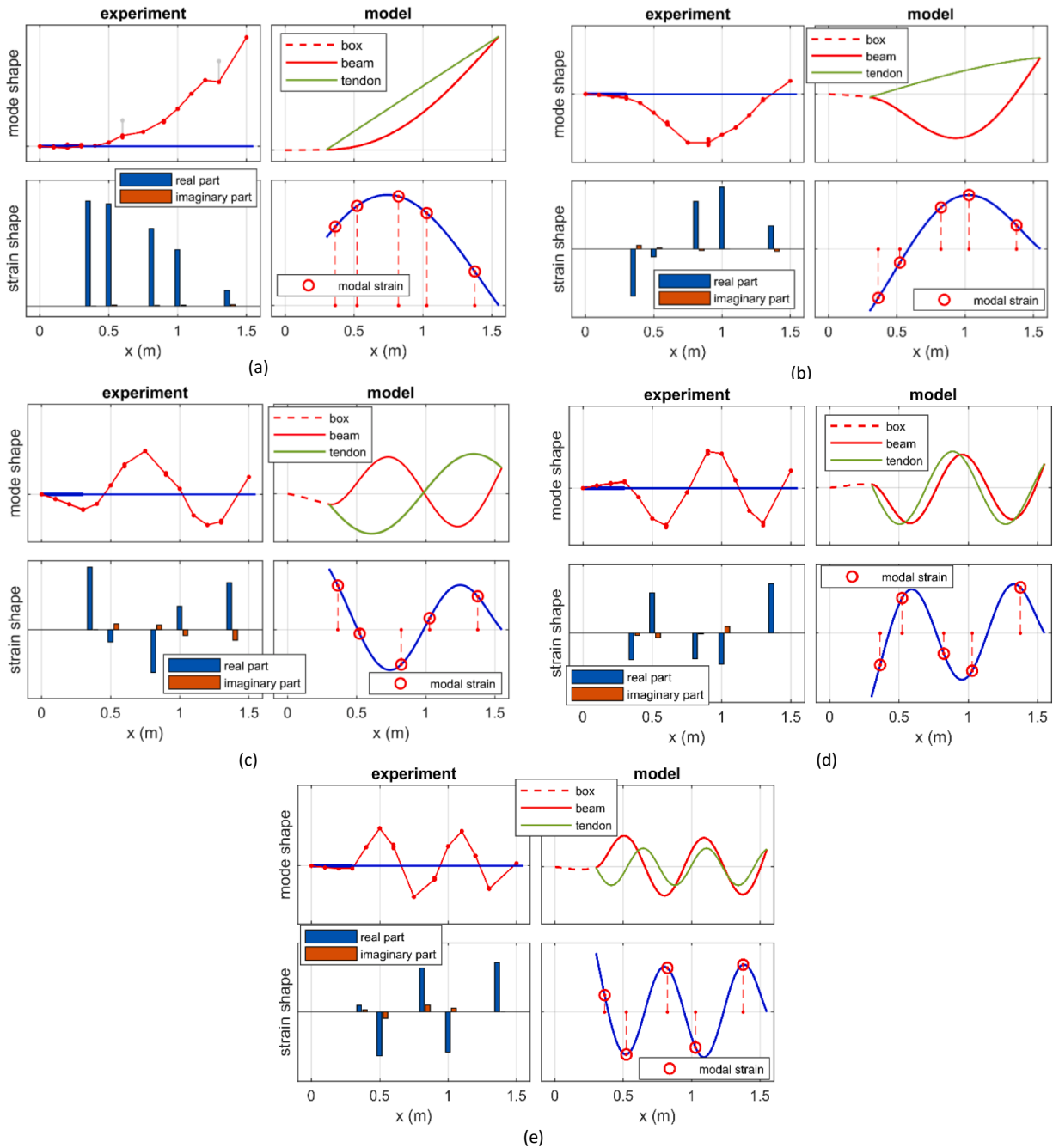


Fig. 9. Model-experiment comparison for (a) B1 mode (experiment: 5.31 Hz / 0.0031, model: 4.50 Hz); (b) B2 mode (experiment: 33.71 Hz / 0.0069, model: 31.42 Hz); (c) B3 mode (experiment: 128.26 Hz / 0.0066, model: 127.13 Hz); (d) B4 mode (experiment: 247.82 Hz / 0.0133, model: 245.16 Hz); (e) B5 mode (experiment: 409.54 Hz / 0.0241, model: 405.00 Hz).

Fig. 9 provides a direct comparison between the identified and modelled modes. The correlation between the two data sets is very good. The obtained relative errors between the predicted and identified frequencies are 15.3%, 6.8%, 0.9%, 1.1%, 1.1% for modes B1, B2, B3, B4 and B5, respectively. The real and imaginary components of the complex strain modes are also shown in Fig. 9. Inspecting these values and noting the small and relatively even participation of the individual complex components, it can be concluded that the damping in the nonrotating test can be approximated using the assumption of the proportional viscous damping.

Fig. 10 shows the identified natural frequencies for all load cases between 0 and 600 N with the increment of 10 N and compares them with the predicted frequencies based on the parameter values given in Table 2. The compared set of modes includes the beam-dominated modes B1 to B5, the box mode, and a set of the tendon-dominated modes (e.g., T1 to T6 for 600 N load case). As expected, the tendon-dominated modes are highly sensitive to the applied loads and, within the considered frequency range, their number increases with the reduced axial loading.

As shown in Fig. 10, the resulting trends agree with those presented in previous research by the authors, e.g., [18,19,21]. The two key observed features are the decrease of the beam-dominated natural frequencies B1 to B5 with the increasing axial loads and the presence of the beam-tendon modal (veering) interactions in the regions where the beam and tendon modal families meet. The maximum axial load considered here was 600 N, which is 68% of the critical buckling load of the system (878 N). Within this loading range, B1 to B5 modes decreased by 22.3%, 17.5%, 5.0%, -0.6% , 1.4%, respectively.

The overall agreement between the predicted and identified natural frequencies across the considered wide range of the loading conditions is satisfactory. The maximum error of 15% observed for mode B1 at 600 N. The typical tendon-dominated mode errors are less than 5%. Torsional mode, indicated by the grey circle markers, is not predicted because the model does not represent this behaviour. The beam dominated box mode is correctly predicted across all loading conditions. The difference between the model and experiment is mainly due to the error in the axial force measurements and oversimplification of the loading box model.

3.2. DLR rotating modal analysis

This section describes the dynamics of the demonstrator when being inserted into the DLR whirl tower. After its insertion, the demonstrator's new equilibrium position differed from the horizontal plane by approximately 8 degrees, pointing downward, see Fig. 3b. When rotating, due to the influence of the centrifugal forces and aerodynamics loads, the beam changed its initial droop angle to a new value of the coning angle α , further closer to the horizontal plane. A dedicated investigation was completed to determine the influence of the boundary rotational spring k_L and nonzero coning angle α . From this and because of the close agreement between the two test setups, a single value of k_L (see Table 2) is used in the rotating studies. Similarly, the influence of the coning angle on the natural frequencies within the range of -8 to 8 deg was found to be negligible and so $\alpha = 0$ deg is adopted.

3.2.1. Load-frequency modal characteristics

The DLR rotating tests are summarised in Fig. 11. This figure shows both identified experimental natural frequencies as well as their predicted counterparts. The focus of this section is the model validation and response analysis. The test plan formulated in Fig. 6 introduced 7 axial loads and 6 rotor speed cases. Complex test conditions under which the experimental modal analysis was completed required additional data recalibration. From this, the identified modal data are attributed to the updated values of the applied axial loads of 0 N, 100 N, 200 N, 290 N, 360 N, 430 N and 500 N.

The operational environment was strongly influenced by the emitted whirl tower noise and various vibrations sources which included both test rig motor/drivetrain and parasitic aerodynamics. To support further analysis, the transfer functions from the piezopatch inputs to the strain gauge outputs (Fig. 5) were analysed with the help of the PolyMAX algorithm. The natural frequencies that were successfully identified are shown as the circles and cross markers for the 64 Hz and 500 Hz excitation range, respectively. To contrast this with the predicted results, and to guide the eye, the computed natural frequencies are shown as solid lines. The

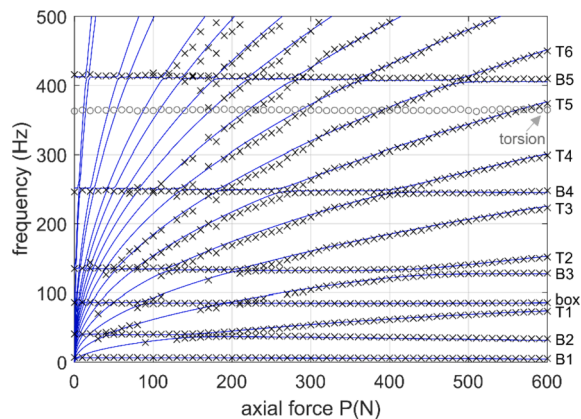


Fig. 10. Natural frequency versus axial load diagram (blue solid line represents the model, black cross and grey circle markers represent experimental results). (For interpretation of the references to colour in this figure legend, the reader is referred to the web version of this article.)

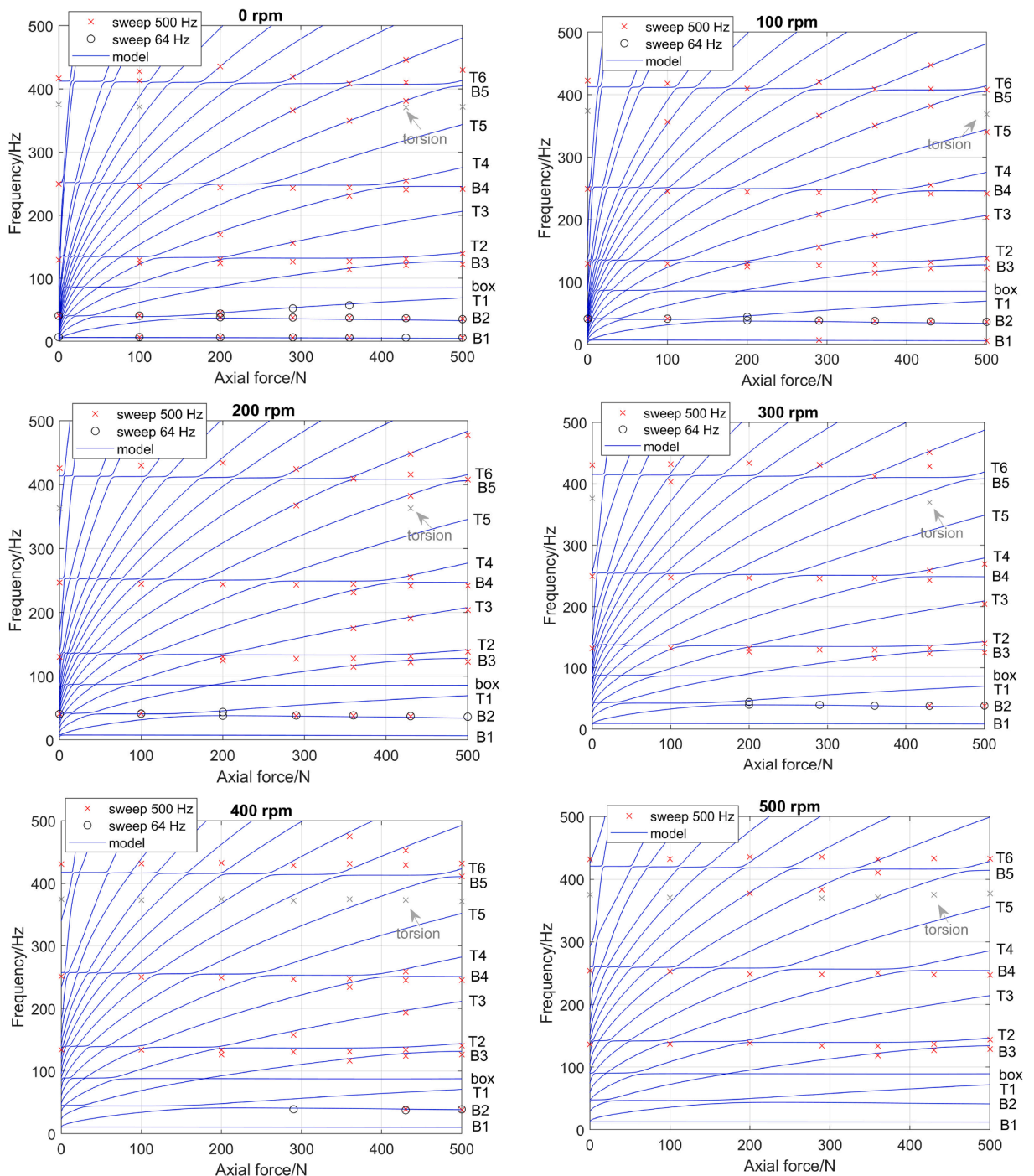


Fig. 11. Summary of the rotating load–frequency modal characteristics (solid lines represent the predicted results, markers represent the identified modal properties).

application of the focused 64 Hz range excitation allowed only moderately improved identification of the modes B1 and B2.

Due to relatively high bending stiffness and low rotor speeds, the rotor harmonics dominated mainly the low frequency range which included B1 and B2 modes. This can be seen in Fig. 11 where the decreasing number of successfully identified instances of B1 and B2 modes can be seen as the rotor speed increases. The frequency range which includes B4 and B5 modes was affected by the secondary damping sources such as the wires, aerodynamic fairing, strain gauges, piezo-patches, taping, etc. Another factor which affected quality of the observed trends in this range is a high number of the beam-tendon veering regions. Consequently, only mode B3 will be used for further focused analysis.

As shown in Fig. 11, the highest number of successfully identified natural frequency points is present at 0 rpm. The tendon dynamics is only identified indirectly around the modal veering regions. For example, the two such regions are visible in Fig. 11 (0 rpm case) between the modes B2 and T1 and between the modes B3 and T2. In particular, the axial load induced B3-T2 interaction is experimentally and analytically captured across all rotor speed cases with a good degree of agreement between the two sets. This result further demonstrates the overall performance of the mathematical model.

These results confirm the anticipated modal trends previously studied in [17–19]. Fig. 11 shows that the beam-dominated natural frequencies decrease globally whilst, due to the beam-tendon coupling, certain detours in the form of the localised frequency rises can be observed too. This is caused by the coupling between the tendon and beam modes with the opposing modal sensitivities when increasing axial loading. Apart from these global trends and inter-modal coupling, both sets of modes increase in response to the centrifugal stiffening. This is shown in Fig. 12, where 0 rpm and 500 rpm cases are mutually contrasted in the reduced frequency range.

Fig. 12a) references the 0 rpm predicted frequencies (blue solid lines) against the 500 rpm case (grey dashed lines). The experimental frequencies (circles and crosses) display a good match with the modelled results as well as general decrease of the beam-dominated frequencies with the applied axial loading. In the similar fashion, Fig. 12b) takes as the reference the 500 rpm case (solid lines) and compares it with the 0 rpm case (grey dashed lines).

The model described in section 2.4 correctly predicts the behaviour introduced through the application of the tendon-based axial loading. Whilst the increasing frequency discrepancies can be observed at higher beam-dominated frequencies (Figs. 11 and 12), it can also be seen that their general magnitude broadly remains the same when changing the loads. This indicates that the tendon is modelled correctly. The difference between the model and experiment can be attributed to the specific modelling fidelity adopted in this work, the error in the axial force measurements and the neglected influence of aerodynamics and whirl tower in the modelling. Further improvements, such as those addressing the loading box interface effects, are straightforward extension of the present modelling methodology.

3.2.2. Influence of rotor speed on natural frequencies

Selected results are shown in Fig. 13 to illustrate the natural frequency changes arising due to the varying rotor speed. Campbell diagrams (the relationship between the rotor speed and the natural frequencies) for the minimum and maximum loading, including the 64 Hz and 500 Hz experimental sweeps as well as the computed beam-tendon frequencies, are included in this figure.

The applied tension increases the effective stiffness of the tendon. This effect can be seen in Fig. 13a) and b) when the sensitivity of the predicted tendon-dominated frequencies is compared between the 0 and 500 N cases. The increased effective stiffness leads to the reduced sensitivity to the centrifugal stiffening resulting from the speed variations. Consequently, the resulting speed-induced tendon modal sensitivities are comparable to those of the beam-dominated modes with possible useful implications for the practical application of the concept.

3.2.3. B3 mode analysis

This section presents focused analysis of the third bending-dominated mode B3. Fig. 14 summarises its changes when varying axial loading and rotor speeds in the form of the natural frequency versus damping ratio points. To maintain focus on global trends, the relationships between the computed and measured results in Fig. 12 were used to select only those results that are the least affected by modal veering. The results are provided as the rotor speed specific polygonal curves. Due to this selective strategy, each polygonal curve consists of four to five points. Further, each point is labelled with the axial load normalised by the maximum axial load considered (500 N) rounded to the one significant digit.

The increasing axial loading causes reduction of the B3 frequency while the rotor speed increase causes the opposite effect. Small

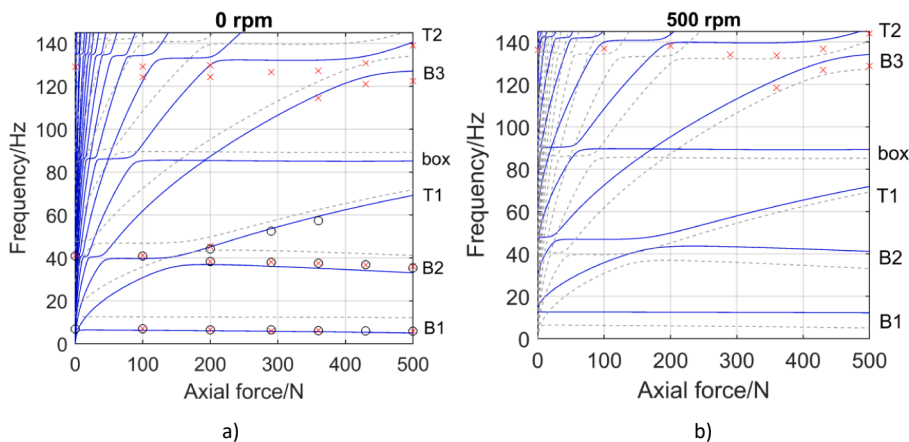


Fig. 12. Combined effect of axial loading and variable rotor speed (dashed lines represent 500 rpm case included in 0 rpm subplot a) and vice versa; solid lines represent the computed frequencies and markers represent the identified modal properties).

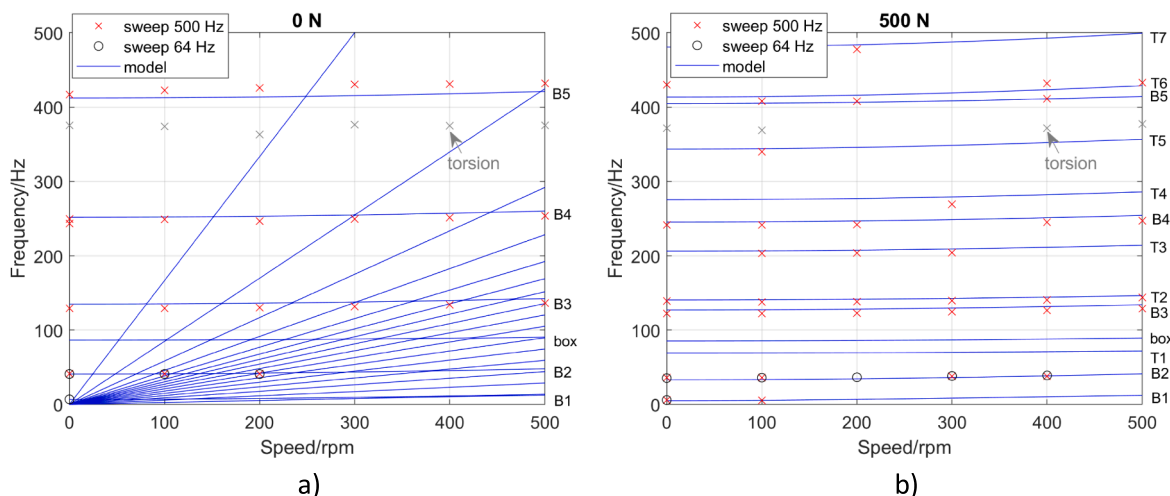


Fig. 13. Selected examples of Campbell diagrams for two different loading regimes.

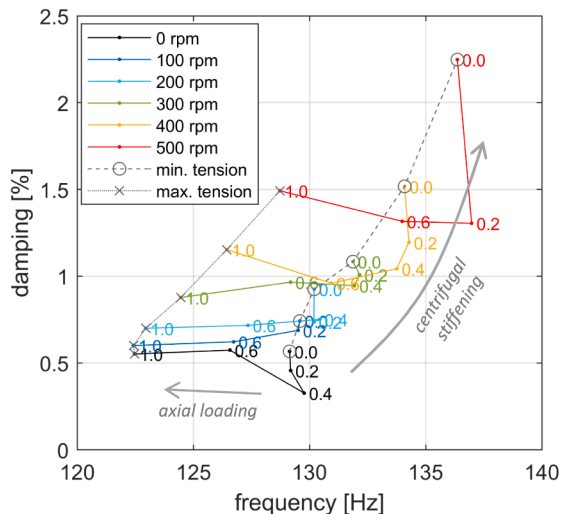


Fig. 14. B3 mode under the combined influence of varying axial loading and rotational speed.

deviations from this behaviour can be observed in the proximity of the lower axial loading regions which are marked by relative insensitivity of the B3 frequency combined with irregular changes in the modal damping. These effects can be attributed to modal veering which, despite the selective nature of the data, is unavoidable in the low loading regions due to the high modal density of the tendon-dominated modes (see Fig. 11). The anticipated frequency reduction trends are observed only after around 40% value of the maximum load considered here.

The initial modal damping changes are thought to be the direct consequence of the reduced beam-tendon rubbing in the system when the tendon is increasingly taut. The value of 0.66% for the B3 modal damping identified during the nonrotating tests (Fig. 9(c)) correlates well with the values observed at 0 rpm, Fig. 14. This value forms the initial structural damping which, when increasing the rotor speed, is seen to gradually change to the values around 1.5%. It can be observed that the dominant factor causing the damping increase is rotation. Overall, each polygonal curve retains its key characteristics with increasing rotor speed. Several effects are assumed to influence this damping behaviour such as the compounded effect of the centrifugal stiffening and increasing aerodynamic damping as well as the increased internal quasi-static loading due to the centrifugal effects.

Following discussion focuses on the veering interactions previously observed in Figs. 11 and 12. Fig. 15 presents the changes of the modal branches in the relevant region of the frequency-damping diagrams where mode B3 interacts with mode T2. Each rotor speed is shown independently and, based on Fig. 11, only in the limited loading range between 290 N and 500 N. The circle markers represent the loading case which correlates the two modal branches shown in each subplot. In each subplot, the mean value and standard

deviation of the damping data, determined for the beam-dominated modal damping values across the full loading range, are included using the solid and dotted horizontal lines.

In agreement with previous discussion, both the mean value and standard deviation generally increase with the increasing rotor speed. An inset illustrates the veering trajectories expected under the influence of the increasing axial load. The identified modal loci display these frequency variations. It can be seen that the modal damping values move in the opposite directions while modes B3 and T2 exchange their modal activity and energy dissipation characteristics. Whereas this behaviour is generally preserved, both high loading and rotor speeds distort these trends as can be seen in the 500 rpm example and the initial damping values of T2 dominated mode.

The final part of this section is dedicated to a discussion of the identified strain mode shape B3 and its complexity. Fig. 16 demonstrates the influence of the axial loading and rotation on this mode.

Mode B3 is shown to be relatively insensitive to the applied conditions. This can be seen in Fig. 16 where each complex strain mode shape is shown such that the strain gauge 1 is unit normalised and the real components are displayed as the vertical quantities while the imaginary parts reside on the horizontal plane. When the non-rotating unloaded case is taken as a reference, the Modal Assurance Criterion is within the range of 0.97 and 0.99. The identified mode shapes are consistent with that shown in Fig. 9. The nonrotating case (blue lines) indicates predominantly normal waveform while the rotating cases (red lines) indicate increasingly complex waveforms.

4. Summary

This work summarised the concept validation activity completed through the collaboration between the University of Bristol (UK) and DLR Braunschweig (Germany) within the framework of the EU-funded Horizon 2020 SABRE project. The active tendon concept was assessed experimentally and analytically.

The results show that the concept demonstrator, which included a new tendon control mechanism, was able to confirm the anticipated load-dependent dynamics which manifested through changes in the beam-dominated vibration mode family. The associated modal frequencies decreased with increasing axial loads. The beam-tendon modal veering was also observed and confirmed the results given in [17–19,21]. Compared to previous research, e.g. [19,21,24], two new modes were found in the investigated frequency range. The presence of these modes was found not to pose any obstacles when studying the principal features.

The instrumented demonstrator allowed extensive modal identification during rotating tests. The mathematical model, which was validated for widely changing tests conditions, was further used to support the analysis where limited experimental data were available. These tests confirmed both the rotation dependent and loading induced dynamic attributes previously observed only in model and nonrotating experiments. Due to its reliable and consistent behaviour, B3 mode was used for the detailed modal analysis with particular focus on modal veering between B3 and T2 modes, induced damping effects and the identified modal behaviour. The analysis showed that this phenomenon involved the damping mechanism exchange when transiting through the veering region. The identified complex strain modes were found to be insensitive to the applied parameter changes and strongly dominated by the normal (real) parts of the modes.

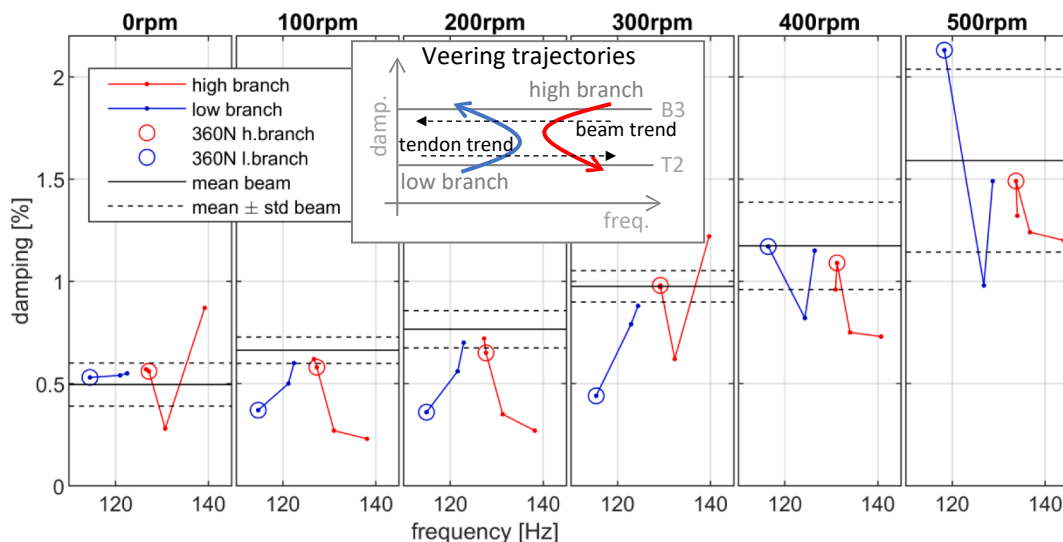


Fig. 15. Modal veering between B3 and T2 mode shown in the frequency-damping diagrams between 290 N and 500 N axial loads and across the full rotor speed range.

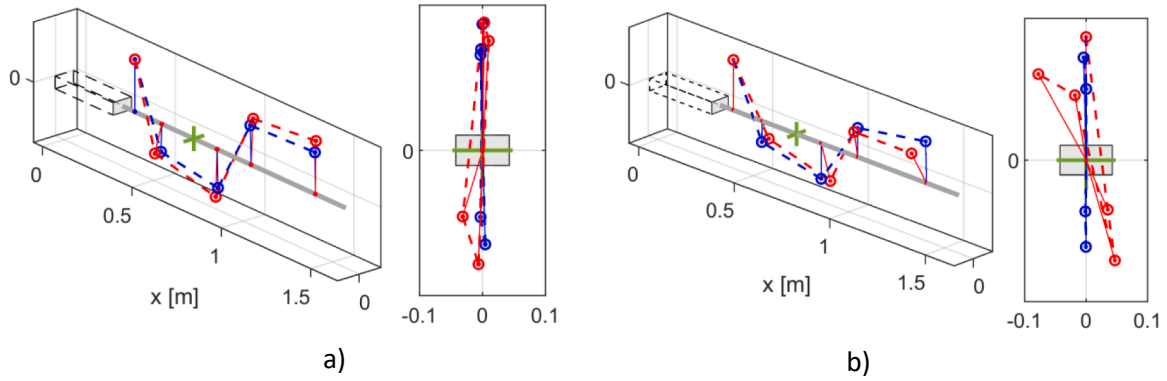


Fig. 16. The influence of rotor speed and axial loading on the strain mode shape B3 (blue is 0 rpm case, red is 500 rpm case, green is the input location): a) 0 N case, b) 500 N case. (For interpretation of the references to colour in this figure legend, the reader is referred to the web version of this article.)

5. Conclusions

A dedicated active tendon demonstrator was designed to validate the active tendon concept in the rotating state and the corresponding mathematical model of the demonstrator was developed. Some conclusions can be drawn as follows.

This research achieved its objectives. The newly developed load delivery mechanism enabled stable application of the loads in the rotating vibrating system. This work shows that the tendon-based axial loads can be used to alter the dynamics in the rotating frame. It is observed that the rotating system features anticipated modal dynamics in the form of centrifugal stiffening and compressive softening of the beam-dominated modes, whilst the tendon-dominated modes display rapid stiffening effects with the applied axial loads. As a result of these opposing trends, further interactional phenomena such as modal veering are observed experimentally and in model-predicted results. One consistently observed beam-dominated mode is used to extend the range of the experimental observations beyond those supported by the models toward the damping characterisation throughout the veering interactions and complex strain mode analysis. The developed mathematical models have sufficient predictive capability to be used both to indicate the unanticipated system dynamics and to complement the experimental results efficiently. Specifically, the model shows a good agreement with the experiment in terms of the frequency-loading diagrams, Campbell diagrams, the mode shapes and strain mode shapes.

This work motivates further directions for the subsequent research, both in the analytical and experimental streams. In particular, further analysis should be extended to the systems with the additional guiding tendon attachments, soft and dynamically tuned attachments, and the sectional locations of the tendon away from the neutral beam (or blade) axis to promote useful static and dynamic coupling mechanisms. Additionally, further experimental improvements can be directed at the introduction of the automated load delivery system, improved axial load sensing and transition from the beam-like to the scaled blade-shaped specimens.

More generally, this research contributes to the understanding of vibrating systems, and interactional dynamics in the coupled systems, which operate in the rotating conditions. In that respect, this work supports improved understanding of various future lift-generating rotating surfaces such as adaptive or morphing rotor blades and blades operating in wide range of performance-optimising conditions.

Declaration of Competing Interest

The authors declare the following financial interests/personal relationships which may be considered as potential competing interests: Johannes Riemenschneider, Brano Titurus reports financial support was provided by Horizon 2020.

Acknowledgements

The authors would like to acknowledge the financial support of the European Community’s Horizon 2020 Program provided through the project “Shape Adaptive Blades for Rotorcraft Efficiency (SABRE)”, Grant Agreement 723491.

Appendix A: Mathematical model

To take into account and assess the influence of new factors such as the presence of the loading box and possibility of the non-zero coning angle introduced through the concept demonstrator and new test conditions, a significantly extended version of the previously developed model [24,27] is outlined here and in section 2.4.

The following vector functions are defined: $W_L(x) = [W_{L1}(x) \ W_{L2}(x) \ \dots \ W_{LN_L}(x)]^T$, $W_B(x) = [W_{B1}(x) \ W_{B2}(x) \ \dots \ W_{BN_w}(x)]^T$, $\Psi_B(x) = [\Psi_{B1}(x) \ \Psi_{B2}(x) \ \dots \ \Psi_{BN_w}(x)]^T$, $W_T(x) = [W_{T1}(x) \ W_{T2}(x) \ \dots \ W_{TN_w}(x)]^T$, $q_L =$

$[q_{L1} \ q_{L2} \ \dots \ q_{LN_w}]$, $q_{Bz} = [q_{Bz1} \ q_{Bz2} \ \dots \ q_{BzN_w}]$, $q_{Br} = [q_{Br1} \ q_{Br2} \ \dots \ q_{BrN_r}]$, and $q_T(t) = [q_{T1}(t) \ q_{T2}(t) \ \dots \ q_{TN_{wt}}(t)]$. The generalised coordinate vector of the system is expressed as $q = [q_L \ q_{Bz} \ q_{Br} \ q_T \ w_P]$.

Three rotation matrices to be used are $T = \begin{bmatrix} \cos\Omega t & \sin\Omega t \\ -\sin\Omega t & \cos\Omega t \\ & & 1 \end{bmatrix}$, $T_0 = \begin{bmatrix} \cos\alpha & -\sin\alpha \\ & 1 \\ \sin\alpha & \cos\alpha \end{bmatrix}$, $\widehat{W} = \begin{bmatrix} 0 & \Omega & 0 \\ -\Omega & 0 & 0 \\ 0 & 0 & 0 \end{bmatrix}$.

The kinetic energy of the loading box is

$$T_L = \frac{1}{2} \dot{q}_L M_L \dot{q}_L^T + \frac{1}{2} q_L \Omega^2 K_L q_L^T + \dot{q}_L G_L \dot{q}_L^T + q_L f_{CL} + \dot{q}_L f_{GL} + T_{L1} \tag{A1}$$

where $M_L = \int_0^{L_1} \int_{A_L} N_L T_0 T_0^T N_L^T \rho_L dAdx = m_L I_{N_L \times N_L}$ is the mass matrix, $N_L = [O \ O \ W_L]$, $\Omega^2 K_L = \int_0^{L_1} \int_{A_L} N_L T_0 \widehat{W} \widehat{W}^T T_0^T N_L^T \rho_L dAdx = \Omega^2 m_L \sin^2 \alpha I_{N_L \times N_L}$ is the centrifugal stiffness matrix, $G_L = \int_0^{L_1} \int_{A_L} N_L T_0 \widehat{W}^T T_0^T N_L^T \rho_L dAdx = O$ is the skew-symmetric gyroscopic coupling matrix, $f_{CL} = \int_0^{L_1} \int_{A_L} N_L T_0 \widehat{W} \widehat{W}^T (T_0^T r_L^T + r_{L0}^T) \rho_L dAdx$ is the vector of generalised centrifugal force, $f_{GL} = \int_0^{L_1} \int_{A_L} N_L T_0 \widehat{W}^T (T_0^T r_L^T + r_{L0}^T) \rho_L dAdx$ is the vector of generalised gyroscopic force, $T_{L1} = \frac{1}{2} \int_0^{L_1} \int_{A_L} (r_L T_0 + r_{L0}) \widehat{W} \widehat{W}^T (T_0^T r_L^T + r_{L0}^T) \rho_L dAdx$ is the kinetic energy of the rigid-body motion, $r_L = (x, y, z)$ is the coordinate of any point in the loading box, $r_{L0} = (L_0, 0, 0)$.

The potential energy of the loading box is

$$U_L = \frac{1}{2} q_L K_{L1} q_L^T + \frac{1}{2} q_L (\Omega^2 K_{L3} - PK_{LP}) q_L^T \tag{A2}$$

where $K_{L1} = \int_0^{L_1} E_L I_{Ly} W''_L W''_L^T dx$, $\Omega^2 K_{L3} = \int_0^{L_1} W'_L W'_L^T C_L(x) \cos \alpha dx$, $K_{LP} = \int_0^{L_1} W'_L W'_L^T dx$, $C_L(x) = \Omega^2 \left[\int_x^{L_1} m_L (x_1 \cos \alpha + L_0) dx_1 + \int_0^{L_2} m_B (x_1 \cos \alpha + L_0 + L_1 \cos \alpha) dx_1 + m_a (L_0 + L_1 \cos \alpha) \right]$.

The kinetic energy of the beam is

$$T_B = \frac{1}{2} \dot{q}_B M_B \dot{q}_B^T + \frac{1}{2} q_B \Omega^2 K_B q_B^T + \dot{q}_B G_B \dot{q}_B^T + q_B f_{CB} + \dot{q}_B f_{GB} + T_{B1} \tag{A3}$$

where $M_B = \int_0^{L_2} \int_{A_B} N_B T_0 T_0^T N_B^T \rho_B dAdx = \begin{bmatrix} m_B I_{N_w \times N_w} & \\ & \rho_B I_{By} I_{N_r \times N_r} \end{bmatrix}$ is the mass matrix, $N_B = \begin{bmatrix} 0 & 0 & W_B(x) \\ -z \Psi_B(x) & 0 & 0 \end{bmatrix}$, $\Omega^2 K_{B4} = \int_0^{L_2} \int_{A_B} N_B T_0 \widehat{W} \widehat{W}^T T_0^T N_B^T \rho_B dAdx = \Omega^2 \left[m_B \sin^2 \alpha I_{N_w \times N_w} \right]$ is the centrifugal stiffness matrix, $G_B = \int_0^{L_2} \int_{A_B} N_B T_0 \widehat{W}^T T_0^T N_B^T \rho_B dAdx = O$ is the skew-symmetric gyroscopic coupling matrix, $f_{CB} = \int_0^{L_2} \int_{A_B} N_B T_0 \widehat{W} \widehat{W}^T (T_0^T r_B^T + r_{B0}^T) \rho_B dAdx$ is the vector of generalised centrifugal force, $f_{GB} = \int_0^{L_2} \int_{A_B} N_B T_0 \widehat{W}^T (T_0^T r_B^T + r_{B0}^T) \rho_B dAdx$ is the vector of generalised gyroscopic force, $T_{B1} = \frac{1}{2} \int_0^{L_2} \int_{A_B} (r_B T_0 + r_{B0}) \widehat{W} \widehat{W}^T (T_0^T r_B^T + r_{B0}^T) \rho_B dAdx$ is the kinetic energy of the rigid-body motion. $r_B = (x, y, z)$ is the coordinate of any point in the beam, $r_{B0} = (L_0 + L_1 \cos \alpha, 0, -L_1 \sin \alpha)$.

The potential energy of the beam is

$$U_B = \frac{1}{2} q_B K_{B1} q_B^T + \frac{1}{2} q_B K_{B2} q_B^T + \frac{1}{2} q_B (\Omega^2 K_{B3} - PK_{BP}) q_B^T + U_{B1} \tag{A4}$$

where $q_B = [q_{Bz} \ q_{Br}]$, $K_{B1} = \begin{bmatrix} O_{N_w \times N_w} & \\ & E_B I_{By} \int_0^{L_2} \Psi'_B \Psi'_B^T dx \end{bmatrix}$, $K_{B2} = \int_0^{L_2} \kappa G_B A_B \begin{bmatrix} W'_B W'_B^T & -W'_B \Psi_B^T \\ -\Psi_B W'_B^T & \Psi_B \Psi_B^T \end{bmatrix} dx$, $K_{B3} = \int_0^{L_2} \begin{bmatrix} W'_B W'_B^T & \\ & O_{N_r \times N_r} \end{bmatrix} \left[\int_x^{L_2} m_B (x_1 \cos \alpha + L_0 + L_1 \cos \alpha) dx_1 + m_P (L_0 + L_1 \cos \alpha + L_2 \cos \alpha) \right] \cos \alpha dx$, $K_{BP} = \int_0^{L_2} \begin{bmatrix} W'_B W'_B^T & \\ & O_{N_r \times N_r} \end{bmatrix} dx$, U_{B1} is a constant energy.

The kinetic energy of the tendon is

$$T_T = \frac{1}{2} \dot{q}_T M_T \dot{q}_T^T + \frac{1}{2} q_T \Omega^2 K_T q_T^T + \dot{q}_T G_T \dot{q}_T^T + q_T f_{CT} + \dot{q}_T f_{GT} + T_{T1} \tag{A5}$$

where $M_T = \int_0^{L_2} N_T T_0 T_0^T N_T^T m_T dx = m_T I_{N_{wt} \times N_{wt}}$ is the mass matrix of the rotating tendon, $N_T = [O \ O \ W_T(x)]$, $\Omega^2 K_{T4} = \int_0^{L_2} N_T T_0 \widehat{W} \widehat{W}^T T_0^T N_T^T m_T dx = \Omega^2 m_T \sin^2 \alpha I_{N_{wt} \times N_{wt}}$ is the centrifugal stiffness matrix, $G_T = \int_0^{L_2} m_T N_T T_0 \widehat{W}^T T_0^T N_T^T dx = O$ is the skew-symmetric gyroscopic coupling matrix, $f_{CT} = \int_0^{L_2} N_T T_0 \widehat{W} \widehat{W}^T (T_0^T r_T^T + r_{T0}^T) m_T dx$ is the vector of the generalised tendon centrifugal forces, $f_{GT} = \int_0^{L_2} N_T T_0 \widehat{W}^T (T_0^T r_T^T + r_{T0}^T) m_T dx$ is the vector of the generalised tendon gyroscopic forces, $T_{T1} = \frac{1}{2} \int_0^{L_2} (r_T T_0 + r_{T0}) \widehat{W} \widehat{W}^T (T_0^T r_T^T + r_{T0}^T) m_T dx$ is the kinetic energy of the rigid-body motion.

$m_T N_T T_0 \widehat{W}^T (T_0^T r_T^T + r_{T0}^T) dx$ is a constant vector, while $T_{T1} = \frac{1}{2} \int_0^{L_2} (r_T T_0 + r_{T0}) \widehat{W} \widehat{W}^T (T_0^T r_T^T + r_{T0}^T) m_T dx$ is the kinetic energy of the rigid-body motion of the rotating tendon. $r_T = (x, 0, 0)$ is the coordinate of any point on the tendon, $r_{T0} = (L_0 + L_1 \cos \alpha, 0, -L_1 \sin \alpha)$.

The potential energy of the tendon is

$$U_T = \frac{1}{2} q_T (\Omega^2 K_{T3} + PK_{TP}) q_T^T \tag{A6}$$

where $K_{T3} = \int_0^{L_2} W'_T W'^T_T \int_x^{L_2} m_T (L_0 + L_1 \cos \alpha + x_1 \cos \alpha) dx_1 \cos \alpha dx$ and $K_{TP} = \int_0^{L_2} W'_T W'^T_T dx$.

The kinetic energies of the tip fixture and the point mass are, respectively,

$$T_P = \frac{1}{2} m_P \dot{w}_P^2 \tag{A7}$$

$$T_a = \frac{1}{2} m_a \dot{w}_B^2(0) = \frac{1}{2} \dot{q}_B^T M_a \dot{q}_B^T \tag{A8}$$

where $M_a = \begin{bmatrix} m_a W_B(0) W_B^T(0) & \mathbf{O}_{N_w \times N_r} \\ \mathbf{O}_{N_r \times N_w} & \mathbf{O}_{N_r \times N_r} \end{bmatrix}$.

The potential energy of the connection between the beam and tendon at the tip via tip fixture is

$$U_{c1} = \frac{1}{2} k [(w_P - w_B(L_2))^2 + (w_P - w_T(L_2))^2] = \frac{1}{2} q K_{c1} q^T \tag{A9}$$

where $K_{c1} = k [V_{Bz}(L_2) - V_P]^T [V_{Bz}(L_2) - V_P] + k [V_T(L_2) - V_P]^T [V_T(L_2) - V_P]$, $V_{Bz}(x) = [\mathbf{O}_{1 \times N_L} \quad W_B(x) \quad \mathbf{O}_{1 \times (N_r + N_w + 1)}]$, $V_L(x) = [W_L(x) \quad \mathbf{O}_{1 \times (N_w + N_r + N_{wt} + 1)}]$, $V_P = [\mathbf{O}_{1 \times (N_L + N_w + N_r + N_{wt})} \quad 1]$.

The potential energy of connection between the loading box and beam is

$$U_{c2} = \frac{1}{2} k (w_L(L_1) - w_B(0))^2 + \frac{1}{2} k_r (w'_L(L_1) - \psi_B(0))^2 = \frac{1}{2} q K_{c2} q^T$$

where $K_{c2} = k [V_L(L_1) - V_{Bz}(0)]^T [V_L(L_1) - V_{Bz}(0)] + k_r [V'_L(L_1) - V_{Br}(0)]^T [V'_L(L_1) - V_{Br}(0)]$, $V_T(x) = [\mathbf{O}_{1 \times (N_L + N_w + N_r)} \quad W_T(x) \quad 0]$, $V_{Br}(x) = [\mathbf{O}_{1 \times (N_L + N_w)} \quad \Psi_B(x) \quad \mathbf{O}_{1 \times (N_{wt} + 1)}]$.

The potential energy of the connection between beam and tendon at the root is

$$U_{c3} = \frac{1}{2} k (w_B(0) - w_T(0))^2 = \frac{1}{2} q K_{c3} q^T$$

where $K_{c3} = k [V_{Bz}(0) - V_T(0)]^T [V_{Bz}(0) - V_T(0)]$.

The potential energy of the connection between beam and tendon via rigid attachments is

$$U_{cf} = \sum_{i=1}^{N_f} \frac{1}{2} k [w_B(x_{ti}) - w_T(x_{ti})]^2 = \frac{1}{2} q K_{cf} q^T$$

where $K_{cf} = \sum_{i=1}^{N_f} k [V_{Bz}(x_{ti}) - V_T(x_{ti})]^T [V_{Bz}(x_{ti}) - V_T(x_{ti})]$, and x_{ti} is the location of i^{th} rigid attachment.

The potential energy of the rotational constraint of the loading box is

$$U_{cL} = \frac{1}{2} k_L w'^2_L(0) = \frac{1}{2} q K_{cL} q^T$$

where $K_{cL} = k_L V'^T_L(0) V'_L(0)$.

All above energy terms can be further handled with the help of the Lagrange's equation of the second kind. The remaining derivation steps are indicated in section 2.4.

Appendix B.: DLR whirl tower characteristics

The rotation can be directed both clockwise and counter-clockwise. The maximum test radius of a specimen is $r_{\max} = 2.5$ m, where the distance from the rotation's centre to the blade mounting position at the rotor arm is $\Delta r = 0.275$ m.

Two HBM type U3 Force Transducer load cells (x- and y- direction) attached to the test bench enable a balance-monitoring during the test runs (channels 14–15 in Fig. 4). Additionally, the mounted velocimeters of the Chadwick-Helmuth VIBREX 2000 balancing system give complementary data. An HBM type U2 load cell shown in Fig. 4 gives information about the motor's torque (channel 16). An incremental rotary-encoder Heidenhain ERN 420, which is connected to the rotating shaft of the test rig, gives data on the rotational speed (channel 13). An AXIS Q6125-LE PTZ CMOS camera, which is mounted at the test chamber's ceiling, provides HDTV 2 MP resolution footage on the overall test setup.

The rotor head is equipped with three potentiometers that measure the blade arm's pitch-, lag- and flap angles (channels 10–12). A

GoPro Hero 5 camera located on blade arm and shown in Fig. 3 take videos with 30 fps and a 4 k-resolution of the test specimen during the test runs. A worm-gear-actuator is attached to the blade arm (Fig. 3) and allows quasi-steady pitch adjustments. A telemetry system on the top of the rotor head (Fig. 3) transmits both the rotor's and the demonstrator's signals to the data acquisition system. 14 × KMT32 Mini Telemetry modules for strain gauges and 2 × KMT MT32 Mini Telemetry modules for ICP devices are available. The required telemetry supply voltage is provided by the shaft's GAT MOOG M60 EW2 + SW50 L1-1 slip ring (45 × 24 V 2 A). That slip ring also possesses 5 × 2 kV 2A connections, two of which are used in the presented experiments for the supply of the demonstrator's piezo patch actuators (see connections at the electronic box in Fig. 3). An Ono Sokki FFT Analyzer CF-7200 generates the sine sweeps for the piezo-actuation in a range of $-2.5 \text{ V} < U_{\text{Amp,In}} < 7.5 \text{ V}$, which are amplified by two Trek PZD2000A High Voltage Amplifiers ($-0.5 \text{ kV} < U_{\text{Amp,Out}} < 1.5 \text{ kV}$).

The above-described signals for both the rotating and nonrotating components are connected to a NI PXIe-6355 module with 80 AI, 2 AO and 24 digital I/O channels. This module is integrated in a NI PXIe-8880 controller system. The data monitoring and acquisition is done by NI Flexlogger Software. A complete overview on the signals is given in Fig. 4.

References

- [1] R.G. Kvaternik, T.S. Murthy, Airframe Structural Dynamic Considerations in Rotor Design Optimization, NASA Technical Memorandum 101646 (1989).
- [2] W.A. Welsh, Helicopter Vibration Reduction, Morphing Wing Technologies (2018) 865–892.
- [3] S. Moffatt, N. Griffiths, Structural optimisation and aeroelastic tailoring of the BERP IV demonstrator blade, American Helicopter Society 65th Annual Forum, Grapevine, Texas, 2009.
- [4] R.H. Blackwell, Blade design for reduced helicopter vibration, J. Am. Helicopter Soc. 28 (1983) 33–41.
- [5] M.L. Wilbur, M.P. Mistry, P.F. Lorber, R. Blackwell, S. Barbarino, T.H. Lawrence, U.T.P. Arnold, Rotary Wings Morphing Technologies: State of the Art and Perspectives, Morphing Wing Technologies (2018) 759–797.
- [6] U.T.P. Arnold, D. Fürst, Closed loop IBC results from CH-53G flight tests, Aerosp. Sci. Technol. 9 (2005) 421–435.
- [7] B. Titurus, Vibration Control in a Helicopter with Semi-Active Hydraulic Lag Dampers, J. Guidance Control Dyn. 36 (2013) 577–588.
- [8] D. Han, J. Wang, E.C. Smith, G.A. Lesieutre, Transient Loads Control of a Variable Speed Rotor During Lagwise Resonance Crossing, AIAA J. 51 (2013) 20–29.
- [9] A.E. Karem, Optimum speed tilt rotor, in: U. States (Ed.), 2003.
- [10] J. Rauleder, B.G. van der Wall, A. Abdelmoula, D. Komp, S. Kumar, V. Ondra, B. Titurus, B.K. Woods, Aerodynamic Performance of Morphing Blades and Rotor Systems, AHS International 74th Annual Forum & Technology Display, Arizona, USA, Phoenix, 2018.
- [11] C. Koch, Parametric whirl flutter study using different modelling approaches, CEAS, Aeronaut. J. (2021).
- [12] R.M. Ajaj, M.S. Parancheerivilakkathil, M. Amoozgar, M.I. Friswell, W.J. Cantwell, Recent developments in the aeroelasticity of morphing aircraft, Prog. Aerosp. Sci. 120 (2021).
- [13] R.P. Dibble, B. Titurus, Helicopter rotor blade modal tuning using internal preloads, in: Proceedings of the International Conference on Noise and Vibration Engineering (ISMA 2016), 2016.
- [14] L.N. Virgin, R.H. Plaut, Effect of axial load on forced vibrations of beams, J. Sound Vib. 168 (1993) 395–405.
- [15] J. Du Bois, N. Lieven, S. Adhikari, Adaptive passive control of dynamic response through structural loading, in: 48th AIAA/ASME/ASCE/AHS/ASC Structures, Structural Dynamics, and Materials Conference 2007.
- [16] R. Dibble, V. Ondra, B. Titurus, Resonance avoidance for variable speed rotor blades using an applied compressive load, Aerosp. Sci. Technol. 88 (2019) 222–232.
- [17] V. Ondra, B. Titurus, Free vibration analysis of a rotating pre-twisted beam subjected to tendon-induced axial loading, J. Sound Vib. 461 (2019).
- [18] J. Wu, B. Titurus, Modal analysis of a rotating pre-twisted beam axially loaded by an internally guided tendon, J. Sound Vib. 498 (2021).
- [19] V. Ondra, B. Titurus, Theoretical and experimental modal analysis of a beam-tendon system, Mech. Syst. Sig. Process. 132 (2019) 55–71.
- [20] V. Ondra, B. Titurus, Theoretical and experimental free vibration analysis of a beam-tendon system with an eccentrically placed tendon, Thin-Walled Struct. 144 (2019).
- [21] V. Ondra, B. Titurus, Free vibration and stability analysis of a cantilever beam axially loaded by an intermittently attached tendon, Mech. Syst. Sig. Process. (2020).
- [22] Z. Bazant, L. Cedolin, Stability of Structures: Elastic, Inelastic, Fracture and Damage Theories, World Scientific, 2010.
- [23] L. Virgin, Vibration of axially-loaded structures, Cambridge University Press, 2007.
- [24] J. Wu, B. Titurus, Damping augmentation of a rotating beam-tendon system via internally placed spring-damper elements, J. Sound Vib. (2021).
- [25] B. Peeters, H. Van der Auweraer, P. Guillaume, J. Leuridan, The PolyMAX frequency-domain method: a new standard for modal parameter estimation? Shock Vib. 11 (2004) 395–409.
- [26] E. Balmès, Frequency domain identification of structural dynamics using the pole-residue parametrization. Proceedings of the Fourteenth International Modal Analysis Conference, 1996.
- [27] J. Wu, B. Titurus, Vibration control of a rotating Timoshenko beam-tendon system via internal guiding inerter-dampers, J. Sound Vib. (2021).
- [28] J. Wu, Y. Qiu, Modelling of seated human body exposed to vertical, lateral and roll vibration, J. Sound Vib. 485 (2020).